Inorganic Chemistry
ARTICLE
pubs.acs.org/IC

Structural Properties of Lithium Thio-Germanate Thin Film Electrolytes Grown by Radio Frequency Sputtering

Inseok Seo and Steve W. Martin*

Department of Materials Science and Engineering, Iowa State University, 2220 Hoover Hall, Ames, Iowa 50011, United States

ABSTRACT: In this study, lithium thio-germanate thin film electrolytes have been successfully prepared by radio frequency (RF) magnetron sputtering deposition in Ar gas atmospheres. The targets for RF sputtering were prepared by milling and pressing appropriate amounts of the melt-quenched starting materials in the $n\mathrm{Li_2S} + \mathrm{GeS_2}$ ($n = 1$, 2, and 3) binary system. Approximately 1 μm thin films were grown on Ni coated Si (Ni/Si) substrates and pressed CsI pellets using 50 W power and 25 mtorr (~3.3 Pa) Ar gas pressures to prepare samples for Raman and Infrared (IR) spectroscopy, respectively. To improve the adhesion between the silicon substrate and the thin film electrolyte, a sputtered Ni layer (~120 nm) was used. The surface morphologies and thickness of the thin films were determined by field emission scanning electron microscopy (FE-SEM). The structural properties of the starting materials, target materials, and the grown thin films were examined by X-ray diffraction (XRD), Raman, and IR spectroscopy.

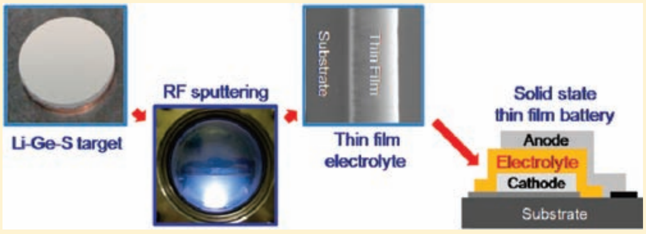

1. INTRODUCTION

One of the important challenges of the future is to develop renewable energy systems for energy conversion, storage, and distribution for use in portable electronics, communications, and transportation. The enormous increase in the demand for energy sources over the past decades has generated a large need for high energy density portable energy sources. As power requirements become more demanding, batteries are also expected to provide higher energy densities. Lithium-based batteries have begun to fill this need because of their use of lithium as the active anode material. Lithium has low density and has a high electrochemical equivalency so that rechargeable lithium batteries are attractive for numerous reasons: high voltages, high energy densities, wide operating temperature ranges, good power density, flat discharge characteristics, and excellent shelf life.

Lithium batteries based upon lithium metal anodes in contact with liquid electrolytes, however, have failed in some cases because of serious safety issues.[1] Lithium metal tends to form dendrites during charging and discharging because of a reaction between lithium metal and liquid/polymer electrolytes.[2] In addition, as the increasing tendency of many advanced technologies is toward miniaturization, the future development of batteries is aiming at smaller dimensions with higher power densities. The development of technologies and miniaturization in the microelectronics industry has reduced the power and current requirements of electronic devices. Therefore, thin film batteries are of interest in small power electronics such as smart cards and other CMOS-based integrated circuit applications.[3,4] Solid state batteries are also attractive in applications such as electric and hybrid vehicles.[5,6] In addition, thin film batteries have lower temperature dependencies and are able to resolve many of the safety issues of lithium batteries using liquid electrolytes.[7] It is being widely recognized that all-solid-state energy devices can be promising for improving the safety and reliability of lithium batteries.

Although thin film batteries have a number of advantages over other battery systems, to succeed in being applied commercially, solid electrolytes with improved ionic conductivities are required. Thin film batteries have been studied for many years and thin film solid state batteries using LiPON (lithium phosphorus oxy-nitride) solid electrolytes have become commercial products.[8,9] LiPON thin films have been shown to have good stability in contact with lithium and have high cyclability.[10] However, this easily prepared material has a relatively low $\mathrm{Li^+}$ ion conductivity of $\sim 10^{-6}$ (S/cm) at 25 °C as compared to other solid electrolytes such as sulfides whose $\mathrm{Li^+}$ ion conductivities are in the range of 10^{-3} (S/cm) at 25 °C.[11−13]

Lithium containing thio-materials show higher ionic conductivities than corresponding oxide materials and as a result much research is being performed to investigate the use of thio-materials as solid electrolytes.[14] However, sulfide materials are very hygroscopic and must be protected from reaction with air so that most studies of these materials have to be conducted in gloveboxes. Sulfide materials such as $\mathrm{SiS_2}$,[15,16] $\mathrm{GeS_2}$,[17] $\mathrm{P_2S_5}$,[18] and $\mathrm{B_2S_3}$[19,20] have been investigated. While much research has been done on ion-conducting bulk sulfide glasses prepared by melt quenching, only a few studies of thin film ion conducting sulfides have been reported[21,22] because of the difficulty in preparing them. Several thin film techniques such as PLD,[23] RF sputtering,[24] e-beam evaporation[25] and PVD[26] have been used to produce thin films. Among these techniques, sputtering techniques have been shown to produce high quality thin films.

In a previous study,[27] sulfide thin films where shown to be oxidized during sputtering which may have occurred because of

Received: July 20, 2010
Published: February 16, 2011

air leakage into the RF chamber. In addition, sulfide thin films can be oxidized in the oxygen contaminated glovebox used to handle the thin films. Another study reported that Li deficiency occurred in the thin films after sputtering compared to that of the target material.[22] Because sulfide thin films are sensitive to moisture and air, it is difficult to characterize their structures, surface morphologies, and electrochemical properties.

In this research, among many possible sulfide materials, GeS_2 is used as the base material because it is less hygroscopic than other sulfides and thus GeS_2 enables a more electrochemically and environmentally stable system to be prepared. While Kim et al.[28] and Itoh et al.[29] reported on the $Li_2S + GeS_2$ bulk glass system, detailed characterizations of thin films in this system have not been reported to date.

In this study, the starting materials, GeS_2 and Li_2S, and the target materials, Li_2GeS_3, Li_4GeS_4, and Li_6GeS_5, were characterized by X-ray diffraction to verify the phase purity of the targets used to produce the films. Further structural characterization of the starting materials, target materials, and their thin films sputtered by RF sputtering in Ar atmosphere was conducted by Raman and IR spectroscopy to verify purity, contamination, and how consistent the structures between targets and their thin films. Finally, the surface morphology and the thickness of the thin films were characterized by field emission scanning electron microscopy (FE-SEM).

2. EXPERIMENTAL METHODS

2.1. GeS_2 Preparation a Starting Material. Glassy GeS_2 was prepared by reacting stoichiometric amounts of germanium metal powder (Alfa, 99.999%) and sulfur (Alfa, 99.999%) in an evacuated silica tube at 900 °C. First, a bare silica tube was cleaned with a 2% aqueous ammonium bifluoride, NH_4HF_2, solution and then rinsed with deionized water. The tube was then fitted with a valve assembly and evacuated to 30 mtorr (~4 Pa) through a liquid nitrogen trap using a roughing pump. Surface moisture on the inside of the tube was then removed by passing the tube over a natural gas/oxygen flame under vacuum. Once this moisture was removed, the tube was transferred to a high quality glovebox (<5 ppm H_2O and <5 ppm O_2) where a mixture of appropriate amounts of Ge and S were placed into the tube. The tube was then reconnected to the valve closed assembly and removed from the glovebox and evacuated with the roughing pump again to a pressure of ~15 mtorr (~2 Pa). Following evacuation, the tube was sealed using a high-temperature natural gas/oxygen torch.

The sealed tube was then placed into a furnace held at an angle of 5° where it was heated at a rate of 1 °C/min from room temperature to 900 °C. The tube was rotated at about 7 rpm to promote mixing and reaction of the components. After the tube was held at 900 °C for 16 h, it was air quenched to room temperature. The air quenched GeS_2 material inside the silica tube was put into the glovebox, and the silica tube was broken to remove the GeS_2 glass product. The final product from this process was a homogeneous transparent and yellow glass. The GeS_2 bulk glass was ground by a vibratory Spex mill for 15 min to make fine powder.

2.2. Preparation of Target Materials. To make the Li_2GeS_3, Li_4GeS_4, and Li_6GeS_5 (n = 1, 2, and 3) target materials, stoichiometric amounts of Li_2S (Alfa, 99.9%) and GeS_2 (as prepared above) powders were used. Inside the glovebox, these powders were vibratory Spex milled for 15 min in a steel container with one steel grinding ball to ensure good mixing and to start the reaction process. Batches of 3 to 4 g were melted in a covered vitreous carbon crucible at 950 °C for 15 min inside a mullite tube lined muffle furnace, attached hermetically to the side of a glovebox. The melted charge was poured out of the crucible onto a brass plate and allowed to cool to room temperature. Once enough material, ~15 g, was prepared the material was vibratory Spex milled for 15 min. Fifteen grams of the powder was weighed out and transferred poured into a hardened 2″ diameter steel die set. The die set was agitated to make the powder as level and as smooth as possible. The top press was placed into the die set and allowed to settle on top of the powder. This assembly was sealed inside a plastic bag to prevent contamination (oxidation) during the consolidation process and taken outside the glovebox to be uniaxially pressed. The die set assembly was placed with a sheet of 1/4″ rubber between the press and the die set and loaded and held at 30,000 lb (~9,000 psi or ~62 MPa) overnight.

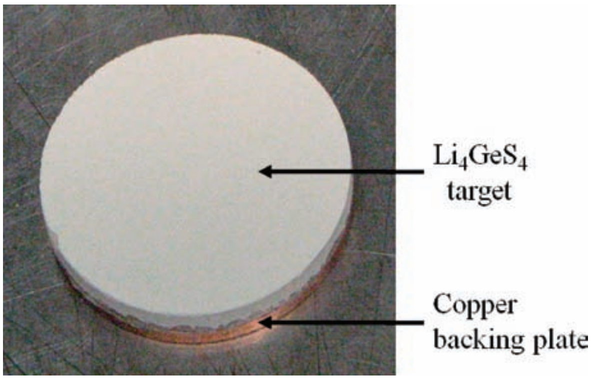

Figure 1. 2″ lithium thio-germanate target attached onto the copper plate using silver paste.

The target was then adhered to a 2″ diameter and 0.125″ thick copper backing plate using silver paste so that it could be water-cooled during the RF deposition process to prevent overheating as shown in Figure 1. Figure 1 shows a picture of 2″ diameter target which was attached onto a copper plate using silver paste.

2.3. Preparation of Ni Coated Si Substrates for Raman Characterization. Single crystal silicon substrates, 1 cm ×1 cm × 360 μm, along the [111] plane were put into a "piranha" solution (H_2SO_4/H_2O_2 = 3:1) for 1 h, ultrasonically cleaned with acetone for 20 min, and then rinsed with D.I. water for 20 min. The samples were dried with high purity N_2 gas. The samples were put in a drying oven at 120 °C overnight to dry.

The cleaned silicon substrates were loaded into a d.c. sputtering chamber in the glovebox. A Ni adhesion layer of ~120 nm thickness was grown for 40 min at ~3 nm/min on the surface of the silicon substrates. The Ni adhesion layer (~120 nm) is used to improve the adhesion between the Si wafer and the thin-film. The Ni adhesion layer is also very useful for Raman spectroscopy. In particular, when one characterizes the films using micro-Raman spectroscopy, the dominant silicon peak, ~520 cm^{-1}, appears in Raman spectra unless a barrier layer is used.

2.4. Preparation of CsI Pellet Substrates for IR Characterization. Approximately 300 mg of CsI powder was weighed and the powder was transferred into a 13 mm diameter stainless steel die-set and pressed at ~6,000 psi (~41 MPa). The pressed CsI sample was 13 mm in diameter and ~0.6 mm thick. The CsI pellets were put into a sample jar, and the sample jar was sealed to prevent reaction with moisture and air. The sealed sample jar was moved to the glovebox which was connected to the RF sputtering chamber. The CsI pellet was loaded from the glovebox into the RF magnetron sputtering chamber on which the thin film electrolytes were grown. The CsI pellet provided an IR transparent support through which the IR spectra of the films could be collected.

2.5. Deposition of the Thin Films. To produce the desired thin films, the target assembly was attached to the sputtering gun inside the glovebox attached to the RF sputtering system. The sputtering gun was then removed from the glovebox and quickly attached to the deposition chamber to minimize oxidation of the target. After which the deposition chamber was evacuated to ~7 × 10^{-8} Torr (~9.3 × 10^{-5} Pa). During the initial pump down, the deposition chamber was heated for 2 days using tape heaters to drive off any residual water on the walls of the system. Substrates were then introduced into the deposition chamber from the glovebox via a sliding load-lock track system.

The chamber was filled high purity Ar gas (99.9999%) to ~100 mtorr (~13 Pa), and the plasma was lit by turning on the RF power to the target. Pre-sputtering was performed for 30 min on the target with the substrate shielded to clean the surface of the target of any impurities (oxygen and water) from the brief exposure to the atmosphere.

After pre-sputtering, the shield was withdrawn, and deposition continued to produce thin films. All films were produced with a power of 50 W and a 25 mtorr (~3.3 Pa) dynamic pressure of the Argon sputtering gas for ~4 h.

2.6. X-ray Diffraction. To verify the structural phase of the GeS_2 glass powder, Li_2S crystalline powder and the target materials, powder X-ray diffraction (XRD) data were collected on finely ground samples at room temperature using a Scintag XDS 2000 diffractometer using CuK_α radiation ($\lambda = 1.5406$ Å). It was operated at 40 kV and 30 mA in the 2θ range of 30°−80° in continuous scan mode with step size 0.03° and scan rate 2.0 deg/min. Because GeS_2, Li_2S crystalline powder, and target materials are unstable in air, these powder materials were covered by an amorphous prolene thin film to prevent air contamination during measurements.

2.7. Raman Spectroscopy. The Raman spectra were collected at room temperature with a Renishaw inVia spectrometer using the 488 nm line of an Ar^+ laser at 50 mW power. The instrument was calibrated using an internal silicon reference, and the bands were accurate to within ± 1 cm^{-1}. The samples were placed into a small cup-like plastic sample holder and then covered with clear amorphous tape to prevent air contamination. It was found by using the confocal feature of the Raman microscope that good quality spectra could be obtained by focusing through the tape and directly on the powdered samples of Li_2S, GeS_2, targets, and the thin films. Examination of multiple spots showed that the samples were homogeneous.

2.8. Infrared Spectroscopy. The mid- and far-infrared absorption spectra were recorded in the range of 4000 to 400 cm^{-1} and 750 to 150 cm^{-1}, respectively, using a Bruker IFS 66 V/s spectrometer. The IR spectra of the starting materials, GeS_2 and Li_2S, and target materials were taken using pressed CsI pellets. Approximately 2 mg of each sample was ground with ~100 mg of CsI into a fine powder and pressed into pellets for IR transmission measurements. The IR spectra typically were obtained using 32 scans at 4 cm^{-1} resolution. For the Li_2GeS_3, Li_4GeS_4, and Li_6GeS_5 thin films, the IR spectra were collected on thin films grown as described above on CsI pellet substrates.

3. RESULTS AND DISCUSSION

3.1. X-ray Diffraction of the Starting Materials and Targets. To verify the phase purity, the XRD pattern of GeS_2 glass powder, Li_2S crystalline powder, and the JCPDS data of Li_2S material are shown in Figure 2. While GeS_2 glass powder is verified to be amorphous, Li_2S powder shows several sharp peaks that are compared to the JCPDS XRD data.[30] As shown in Figure 2, the XRD pattern of the Li_2S powder closely matches the JCPDS data. From the JCPDS data, it is verified that the system and space group of Li_2S powder are face-centered cubic and *Fm*3*m*, respectively.

The Li_2GeS_3, Li_4GeS_4, and Li_6GeS_5 target materials were also characterized by XRD, and the data are shown in Figure 3. The Li_2GeS_3 target shows an amorphous pattern without dominant peaks because the melt-quenching technique combined with its 50% GeS_2 glass former composition are sufficient to make this phase amorphous on cooling during preparation. The XRD patterns of the Li_4GeS_4 and Li_6GeS_5 targets, on the other hand, are polycrystalline and show sharp peaks because the Li_4GeS_4 and Li_6GeS_5 targets contain only 33% and 25% of the GeS_2 glass former, respectively, which are not sufficient to vitrify these melts on quenching.

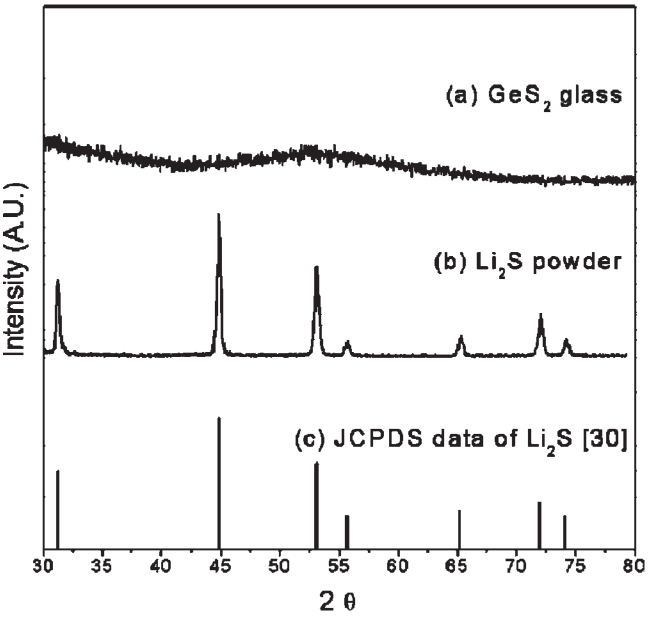

Figure 2. XRD pattern of the starting materials, glassy GeS_2 (a) and polycrystalline Li_2S (b) and compared to the JCPDS data of Li_2S (c).

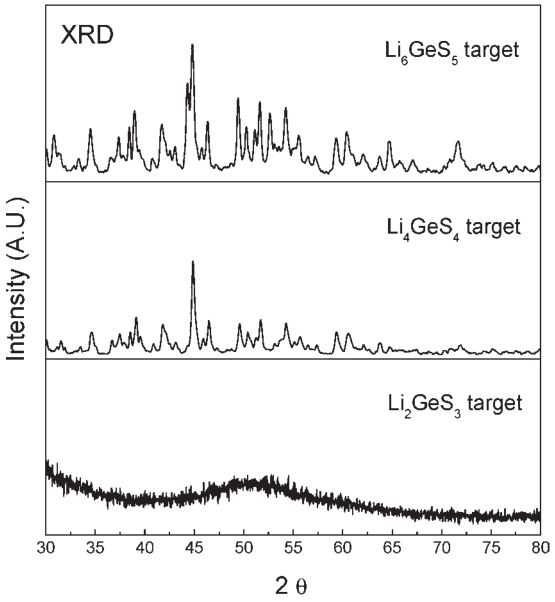

Figure 3. XRD pattern of Li_2GeS_3, Li_4GeS_4, Li_6GeS_5 target materials.

Figure 4 shows XRD pattern of the Li_4GeS_4 target material which was quenched on a brass plate in the glovebox and the reference data[31] of Li_4GeS_4. The XRD pattern of our experimental Li_4GeS_4 target material shows slightly broader peaks than those of the reference data.[31] A possible reason is that the Li_4GeS_4 target contains 33% GeS_2 glass former and was quenched quickly on brass a plate. This rapid quenching presumably produces a more defective crystal structure than typical slow cooled or solid

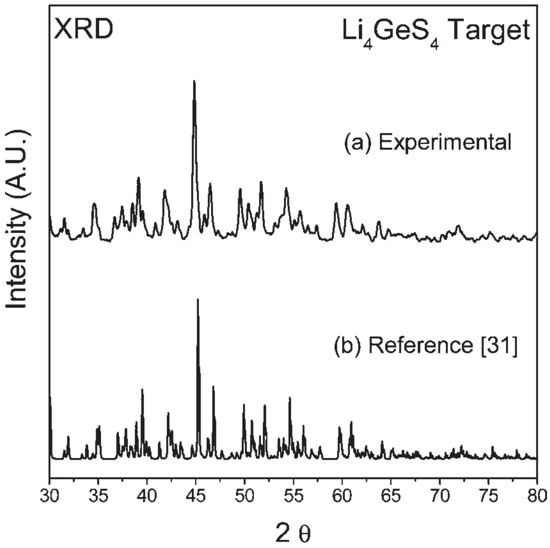

Figure 4. XRD pattern of the Li_4GeS_4 target material (a) and reference data of Li_4GeS_4 (b).

state reaction prepared samples. However, the XRD pattern of the Li_4GeS_4 target material still appears to closely match the reported reference pattern. Murayama et al.[32] reported that the structure of Li_4GeS_4 is related to that of γ-Li_3PO_4 and is composed of hexagonal close-packed sulfide ions with germanium ions distributed over the tetrahedral sites. In this structure, the Li^+ ions are located in both octahedral and tetrahedral sites. Murayama et al.[32] suggested that the distribution of Li^+ ions in the LiS_4 tetrahedra, the interstitial tetrahedral sites, and the LiS_6 octahedra sites forms conduction pathways in the crystal. For this reason, the Li_4GeS_4 material shows higher ionic conductivity than oxide materials.

From Figure 3, it can be seen that the XRD pattern of the Li_6GeS_5 target appears more complex and contains peaks with higher intensities than those of Li_4GeS_4 target. The Li_6GeS_5 composition contains a higher Li_2S content than the Li_4GeS_4, 75 mol % Li_2S versus 67 mol % Li_2S, and for this reason this phase is expected to be an equi-molar mixture of Li_2S and Li_4GeS_4 because as far as can be determined from the literature so far available, Li_6GeS_5 is not a single congruently melting phase. This would cause the XRD pattern to be a mixture of the XRD pattern of Li_2S and Li_4GeS_4. Hence, it is suggested that Li_6GeS_5 is composed of Li_4GeS_4 and Li_2S. To verify that Li_6GeS_5 contained Li_4GeS_4 and Li_2S in the XRD experimental data, Li_2S, Li_4GeS_4, and Li_6GeS_5 XRD data corresponding to the prepared target samples are shown in Figure 5. While XRD data of Li_4GeS_4 do not show peaks related to those of Li_2S, XRD data of Li_6GeS_5 show peaks related to those of Li_2S. The filled stars indicate the peaks of Li_2S, and the filled triangles indicate the peaks of Li_4GeS_4 in the XRD data of Li_6GeS_5. This suggests that the XRD pattern for Li_6GeS_5 agrees well with the expectation that it is composed of equi-molar mixture of Li_4GeS_4 and Li_2S. The Li_4GeS_4 and Li_6GeS_5 targets are crystalline as shown in Figure 3. The fact can also be seen from the Raman spectra in Figure 9. The Li_2GeS_3, Li_4GeS_4, and Li_6GeS_5 thin films were not characterized by XRD because our standard XRD system is not sensitive enough to examine such thin films as are reported here.

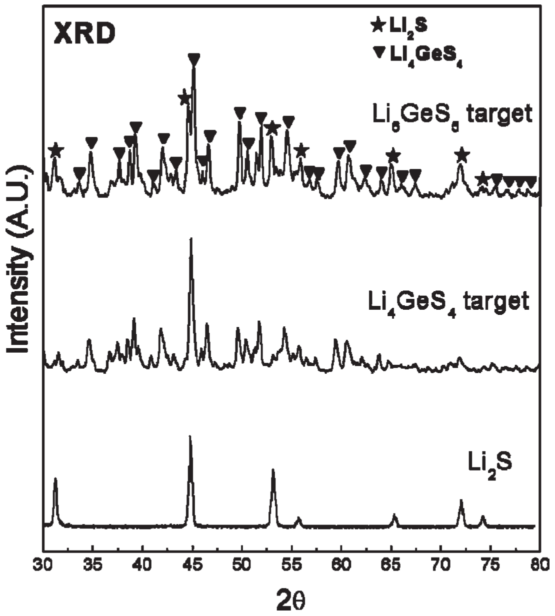

Figure 5. Comparison of XRD pattern of Li_6GeS_5 to that of $Li_2S + Li_4GeS_4$.

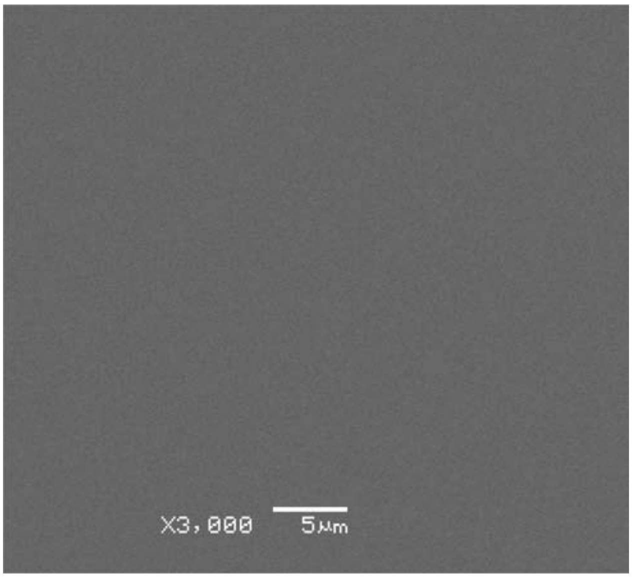

Figure 6. FE-SEM of a Li_4GeS_4 thin film grown on a Ni/Si substrate in an Ar atmosphere.

3.2. Surface Morphology and Thickness of the Thin Film.

Figure 6 shows the surface morphology of the thin films produced in an Ar atmosphere. The thin film surface is mirror-like without any defects or cracks. This suggests that the thin film electrolytes are homogeneous and have a flat surface morphology. The smooth surface enables the thin films to decrease the contact resistance between thin film and the electrodes. To determine the sputtering rate, the thickness of the thin films were measured in the cross-section direction by FE-SEM as shown in Figure 7. The Ni adhesion layer (~120 nm) is used to improve the adhesion between the Si wafer and the thin film. The Ni adhesion layer is also very useful for Raman spectroscopy. In particular, when one characterizes the films using micro-Raman spectroscopy, the dominant silicon peak, ~520 cm^{-1}, appears in Raman spectra unless a barrier layer is used. Therefore, the Ni adhesion layer also acted to prevent the appearance of the peak from the silicon substrate. Furthermore, it has been found that Ni is chemically

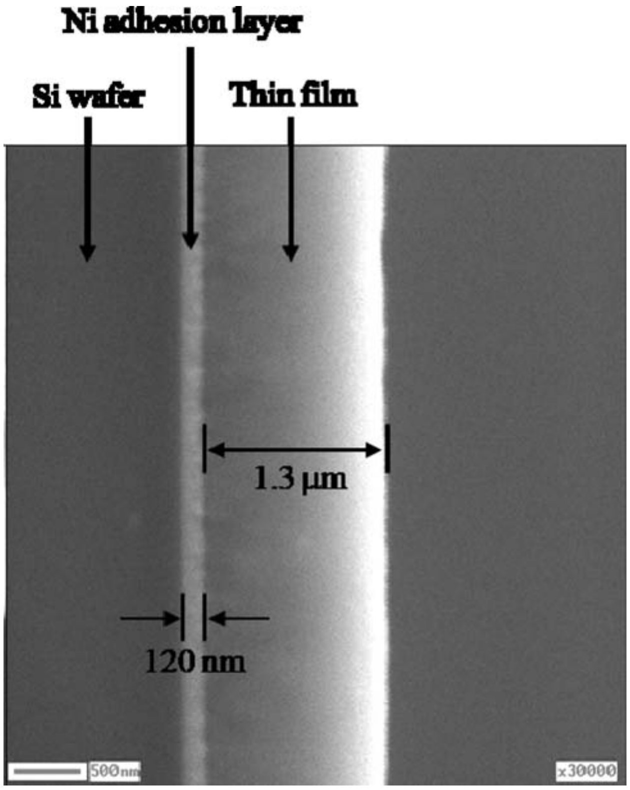

Figure 7. FE-SEM of a cross-sectional view of a Li_4GeS_4 thin film grown on a Ni/Si substrate in an Ar atmosphere.

stable in contact with the lithium thio-germanate thin film electrolytes.[33] The sputtering power and pressure of 50 W and 25 mtorr (~3.3 Pa) were used, respectively, and the total thickness of the thin film after 2 h of sputtering is ~1.3 μm which gives a sputtering rate of ~5 nm/minute.

3.3. Raman Spectroscopy. Starting materials, GeS_2 and Li_2S, were characterized by Raman spectroscopy to analyze their purity and to determine their chemical structure and are shown in Figure 8. In the Raman spectrum of GeS_2, a strong main peak appears at ~340 cm^{-1} that agrees well with that of literature[34] and is assigned to the symmetric stretching of bridging sulfur, S (BS), (Ge−S−Ge) in the $GeS_{4/2}$ tetrahedra. The Raman spectrum of Li_2S shows a single strong peak at ~375 cm^{-1} which is assigned to Li^+S^- stretching modes. The Raman spectrum of the Li_2S is sharper than that of GeS_2 glass because Li_2S is crystalline while the GeS_2 is glassy.

The Raman spectra of the Li_2GeS_3, Li_4GeS_4, and Li_6GeS_5 targets are shown in Figure 9. In the spectrum of the Li_2GeS_3 target, there are three dominant peaks at 340, 375, and 415 cm^{-1}. The peak at 340 cm^{-1} is found in GeS_2 and is assigned to BS (Ge−S−Ge) bonding. The peak at 375 cm^{-1} is found in the Raman spectrum of Li_2S for this reason is assigned to Li^+S^- ionic bonding. The peak at 415 cm^{-1} is assigned to non-bridging sulfur (NBS) ≡Ge−S^- ionic bonding. While there are three peaks in the Raman spectra of the Li_2GeS_3 target, the Raman spectrum of the Li_4GeS_4 and Li_6GeS_5 targets show only one dominant peak at 375 cm^{-1}. The strong main Raman peak in both Li_4GeS_4 and Li_6GeS_5 target materials appears at 375 cm^{-1} which is at the same peak position of Li_2S. This indicates that 375 cm^{-1} peak in both of the target materials was related to that of the Li_2S component. The narrowing of the Raman peaks in the spectra of Li_6GeS_5 and Li_4GeS_4 compounds compared to that of Li_2GeS_3 arises from the polycrystalline structure of the former and the glassy structure of the latter.

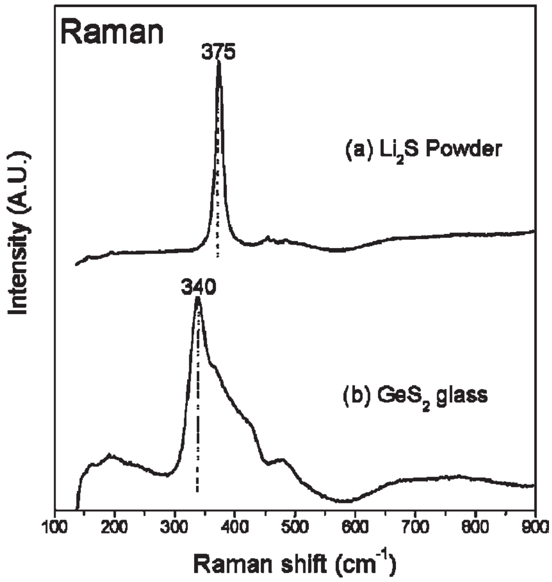

Figure 8. Raman spectra of Li_2S (a) crystalline powder and GeS_2 glass powder (b).

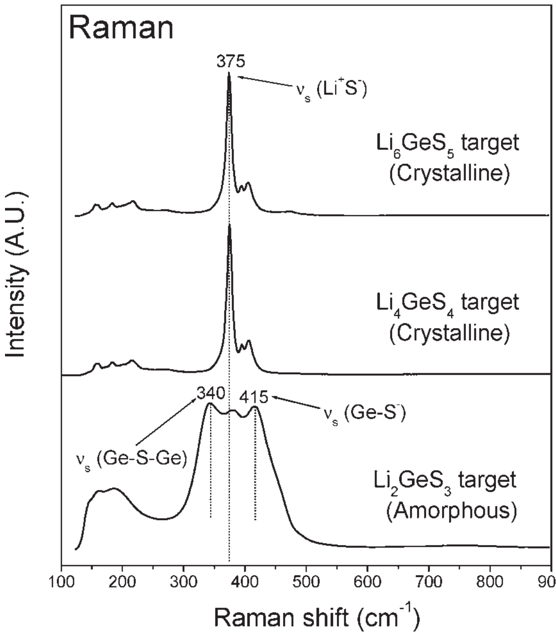

Figure 9. Raman spectra of Li_2GeS_3, Li_4GeS_4, Li_6GeS_5 target materials.

The Raman spectra of the Li_2GeS_3, Li_4GeS_4, and Li_6GeS_5 thin films are shown in Figure 10. The Raman spectrum of the Li_2GeS_3 thin film shows three dominant peaks at 340, 375, and 415 cm^{-1}. The peak at 340 cm^{-1} is coincident with GeS_2 main peak position and is assigned to the BS (Ge−S−Ge) mode. The 375 cm^{-1} peak is assigned to Li^+S^- modes and the 415 cm^{-1} peak is assigned to NBS (Ge−S^-) modes. Among the three peaks, the peak at 340 cm^{-1} has the highest intensity. This is due to the high fractions (50%) of GeS_2 glass former in Li_2GeS_3. The Raman spectrum of the Li_4GeS_4 thin film also shows three peaks

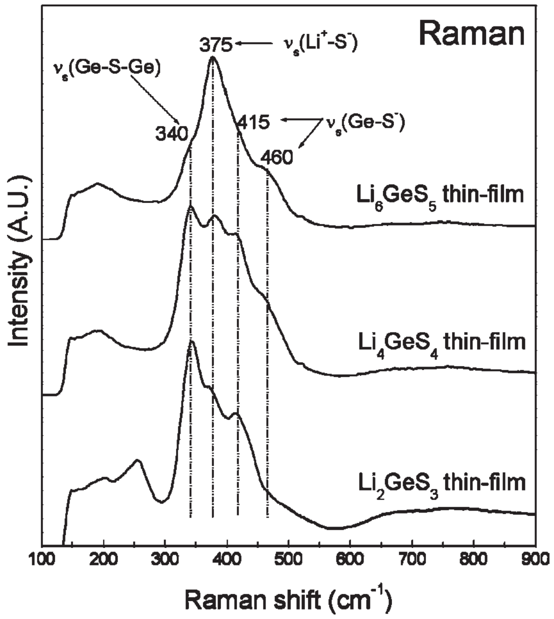

Figure 10. Raman spectra of the Li_2GeS_3, Li_4GeS_4, and Li_6GeS_5 thin films grown in Ar atmosphere on Ni/Si substrate.

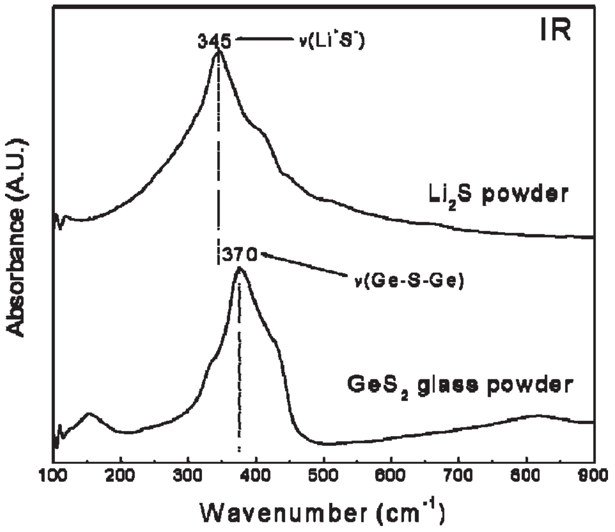

Figure 11. Infrared spectra of the glassy GeS_2 powder and Li_2S crystalline powder starting materials.

at 340, 375, and 415 cm^{-1}, like the spectrum of the Li_2GeS_3 thin film, and another broader peak of lower intensity at 460 cm^{-1}. The intensities of the peaks at 375 and 415 cm^{-1} are higher than those in the spectrum of the Li_2GeS_3 thin film. This is consistent with the increased Li_2S content in the Li_4GeS_4 compared to Li_2GeS_3 which would increase the concentration of both Li^+S^- and Ge−S^- NBS modes. The Raman spectrum of the Li_6GeS_5 thin film which has an even higher Li_2S content compared to the other thin films only has one dominant peak at 375 cm^{-1} which is assigned to the Li^+S^- vibrational mode. This indicates that the Li_6GeS_5 thin film contains the highest Li_2S content compared to the other two thin films. There are three low intensity peaks at 340, 415, and 460 cm^{-1} in the spectrum of Li_6GeS_5. As described above, the peak at 340 cm^{-1} is assigned to the bridging sulfur (Ge−S−Ge bonding), and the peaks at 415 and 460 cm^{-1} are assigned to modes of the NBS (Ge−S^-). The peak at 460 cm^{-1} is assigned to 1 NBS and the peak is not present significantly in thin films. The peak at 415 cm^{-1} is assigned to 2 NBS, and the peak is present in thin films. On the other hand, the peak at 340 cm^{-1} is assigned to 0 NBS, and the peak is present in thin films. The Raman spectra of all of the thin films do not show sharp peaks, but rather show broad peaks compared to those of crystalline targets (Li_4GeS_4 and Li_6GeS_5) and are consistent with the films being amorphous. As the Li_2S content increases in the targets (Li_2, Li_4, and Li_6), the Li_2S content in the thin film increases. It can be concluded that although the previous reported literature showed Li_2S deficiency in GeS_2-based thin films after sputtering compared to that of target,[22] the amount of Li_2S in the thin films in this study increases with the increase of Li_2S in the target and are consistent with the Li_2S content in the targets.

3.4. Infrared Spectroscopy.

To further characterize the starting materials, GeS_2 glass powder and Li_2S crystalline powder, targets, and their thin films were characterized by infrared spectroscopy. Attention is focused on the far-IR region (900 to 100 cm^{-1}) to evaluate the nature of the chemical bonding in the materials, as well as the mid-IR region (4000 to 400 cm^{-1}) to determine how these materials might be contaminated by oxygen and/or moisture before and/or after processing. However, because of the lack of any significant O or OH contamination in the films and the very thin dimension, they were not observed in the mid-IR spectra and for this reason are not shown here. However, in the far-IR region, strong absorptions were observed and arise from the framework structure species Li, Ge, and S.

The IR spectra of the starting materials, polycrystalline Li_2S and glassy GeS_2, are shown in Figure 11. The IR peak in the far-IR spectrum of Li_2S at ~345 cm^{-1} is assigned to the ionic bonding of Li^+S^-, and the strong peak at ~370 cm^{-1} in the spectrum of glassy GeS_2 is assigned to the BS, ν(Ge−S−Ge, BS) mode of the $GeS_{4/2}$ tetrahedra.[35] It is possible that the broad peak in the IR spectrum of GeS_2 can be deconvoluted into two additional peaks, one centered at ~325 cm^{-1} and the other centered at ~435 cm^{-1}. These two additional peaks also arise from vibrational modes of the $GeS_{4/2}$ tetrahedra.[36] The shift wavenumbers can be due to the presence of compressive stress in the film which is expected for films deposited by RF sputtering. In the IR spectra of the GeS_2, there is one peak with broad and low intensity at ~800 cm^{-1}.[35] This peak is assigned to the preparation and handling of the Ge−O bonding mode. It can be assumed that GeS_2 might be slightly contaminated by oxygen during IR sample. In the IR spectra of both the starting materials, there is no peak at ~1500 cm^{-1} (O−H vibration mode) or at ~3500 cm^{-1} (O−H stretching mode), so this suggests that these two starting materials are not significantly contaminated by oxygen or moisture.

The IR spectra of Li_2GeS_3, Li_4GeS_4, and Li_6GeS_4 targets are shown in Figure 12, and all show dominant peaks at ~360 cm^{-1} and 415 cm^{-1} and a low intensity peak at ~750 cm^{-1}. The IR peak at ~360 cm^{-1} is assigned to the BS, ν(Ge−S−Ge, BS) mode and the 415 cm^{-1} peak corresponds to the vibration stretch of Ge with two non-bridging sulfur atoms. The broad IR peak at ~360 cm^{-1} can be deconvoluted into two peaks one centered at 345 cm^{-1} corresponding to Li^+S^- mode and the other centered at ~360 cm^{-1} corresponding to Ge−S−Ge mode. In addition, one low intensity peak which is assigned to oxide impurities, ν(Ge−O−Ge) appears at ~750 cm^{-1}. It is possible that contamination occurs when the target materials are melted in the glovebox because a background level of several

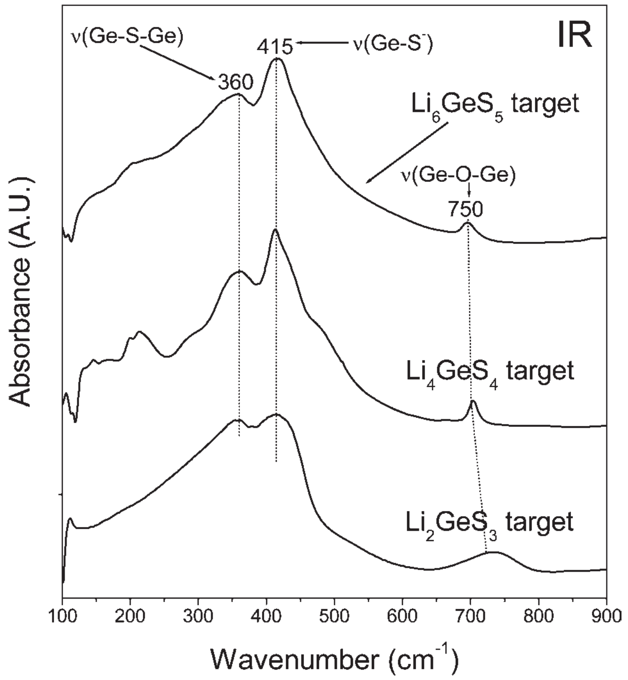

Figure 12. Infrared spectra of the Li_2GeS_3, Li_4GeS_4, and Li_6GeS_5 target materials.

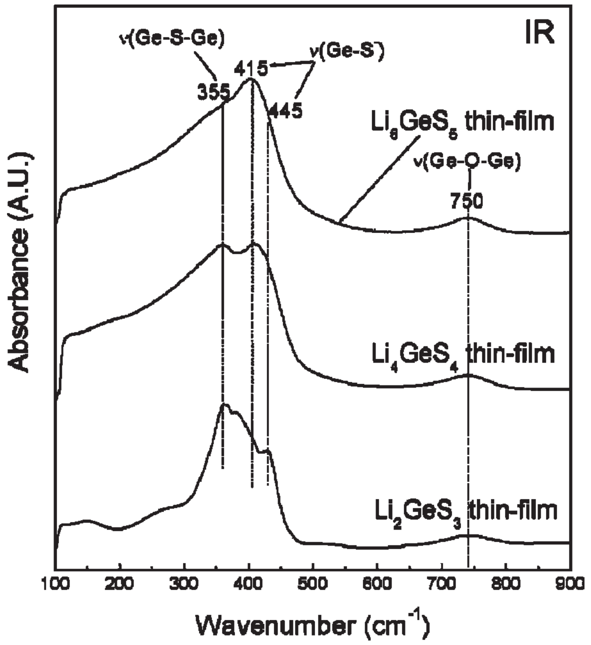

Figure 13. Infrared spectra of the Li_2GeS_3, Li_4GeS_4, and Li_6GeS_5 thin films grown in an Ar atmosphere on a CsI pressed pellet.

ppm O_2 exists in the glovebox. Another possibility is that the oxygen comes from the GeS_2; its spectrum in Figure 10 shows that there is a low intensity peak at ~750 cm^{-1} assigned to GeO_2.

To the best of our knowledge, the IR spectra of the thio-germanate based thin film materials have not been reported in the open literature. In this research, to characterize the thin films by IR spectroscopy, the Li_2GeS_3, Li_4GeS_4, and Li_6GeS_5 thin films were deposited directly on the top side of the pressed CsI pellets that provided a mid- and far-IR transparent support for the films.

The Li_2GeS_3, Li_4GeS_4, and Li_6GeS_5 thin films were deposited directly on the pressed CsI pellets, and the IR spectra were then collected in transmission and are shown in Figure 13. The intense peak at ~360 cm^{-1} can be deconvoluted into two peaks one centered at 345 cm^{-1} corresponding to the Li^+S^- mode and the other centered at ~360 cm^{-1} corresponding to the Ge—S—Ge mode as described above, and the intensity of this peak decreases with added Li_2S. In addition, as shown in Figure 12, one low intensity peak which is assigned to oxide impurities, ν(Ge—O—Ge) appears at ~750 cm^{-1}. A new band appears at 445 cm^{-1} as a result of the formation of non-bridging sulfurs $-Ge-S^-Li^+$ (NBS). This NBS band was reported at ~450 cm^{-1} in the IR spectra of binary xNaS + $(1 - x)GeS_2$ glasses.[37] The NBS band at 445 cm^{-1} diminishes as another NBS band at 415 cm^{-1} grows stronger with further additions of Li_2S, and this suggests that the number of NBS per Ge increases with the addition of Li_2S. Indeed, it is expected from the compositions that these would be 2 NBS in Li_2GeS_3 and 4 NBS in Li_4GeS_4 and Li_6GeS_5.

4. CONCLUSIONS

For the first time, lithium thio-germanate thin film electrolytes for the solid-state lithium-ion batteries grown by RF sputtering were characterized thoroughly by XRD, FE-SEM, Raman, and IR spectroscopy. From the XRD pattern, the Li_2GeS_3 ($n = 1$) target was amorphous and the Li_4GeS_4 ($n = 2$) and Li_6GeS_5 ($n = 3$) targets were crystalline as expected from compositions. The Li_6GeS_5 target appears to be consistent with a equi-molar mixture of Li_2S and Li_4GeS_4. FE-SEM of the thin films deposited on Ni coated Si substrates shows a mirror-like surface without cracks or pits. The Ni adhesion layer acted to improve the contact of the thin films on Ni/Si substrate and acted to prevent Li—Si reaction during sputtering. The Raman spectra of all of the thin films do not show sharp peaks, rather they show much broader peaks compared to those of crystalline targets (Li_4GeS_4 and Li_6GeS_5) and are consistent with the thin films being amorphous. This shows that RF sputtering can be used to extend the formation range of amorphous materials from ~50 mol % Li_2S to ~75%. The Raman and IR spectra also showed the structural and compositional consistency between targets and the thin films and that the Li_2S content of thin films increased as expected with Li_2S addition in the targets. These results suggest that the thin films did not show significant Li deficiency as seen in previous reports after sputtering. The IR spectra of the thin films show a low intensity peak related to Ge—O—Ge at ~750 cm^{-1} and suggests that oxygen contamination of the films occurred during sample preparation and handling. By successfully making thin films of a high quality these lithium thio-germanate thin film electrolytes can be used for solid state thin film Li-ion batteries.

■ AUTHOR INFORMATION

Corresponding Author

*Phone: (515) 294-0745. Fax: (515) 294-5444. E-mail: swmartin@iastate.edu.

■ ACKNOWLEDGMENT

This research was supported by NSF under Grant DMR-0312081, and this research support is gratefully acknowledged.

REFERENCES

(1) Rao, B. M. L.; Francis, R. W.; Christopher, H. A. *J. Electrochem. Soc.* **1977**, *124*, 1490.

(2) Tatsuma, T.; Taguchi, M.; Iwaku, M.; Sotomura, T.; Oyama, N. *J. Electroanal. Chem.* **1999**, *472*, 142.

(3) Albano, F.; Lin, Y. S.; Blaauw, D.; Sylvester, D. M.; Wise, K. D.; Sastry, A. M. *J. Power Sources* **2008**, *185*, 1524.

(4) Souquet, J. L.; Duclot, M. *Solid State Ionics* **2002**, *148*, 375.

(5) Jansen, A. N.; Kahaian, A. J.; Kepler, K. D.; Nelson, P. A.; Amine, K.; Dees, D. W.; Vissers, D. R.; Thackeray, M. M. *J. Power Sources* **1999**, *81*−*82*, 902.

(6) Yang, C.-C.; Hsu, S.-T.; Chien, W.-C. *J. Power Sources* **2005**, *152*, 303.

(7) Tarascon, J. M.; Armand, M. *Nature* **2001**, *414*, 359.

(8) Neudecker, B. J.; Dudney, N. J.; Bates, J. B. *J. Electrochem. Soc.* **2000**, *147*, 517.

(9) Yu, X.; Bates, J. B.; Jellison, J. G. E.; Hart, F. X. *J. Electrochem. Soc.* **1997**, *144*, 524.

(10) Souquet, J. L.; Robinel, E.; Barrau, B.; Ribes, M. *Solid State Ionics* **1981**, *3*−*4*, 317.

(11) Bates, J. B.; Dudney, N. J.; Gruzalski, G. R.; Zuhr, R. A.; Choudhury, A.; Luck, C. F.; Robertson, J. D. *J. Power Sources* **1993**, *43*, 103.

(12) Jones, S. D.; Akridge, J. R. *Solid State Ionics* **1992**, *53*−*56*, 628.

(13) Kondo, S.; Takada, K.; Yamamura, Y. *Solid State Ionics* **1992**, *53*−*56*, 1183.

(14) Pradel, A.; Ribes, M. *Mater. Chem. Phys.* **1989**, *23*, 121.

(15) Aotani, N.; Iwamoto, K.; Takada, K.; Kondo, S. *Solid State Ionics* **1994**, *68*, 35.

(16) Kennedy, J. H.; Yang, Y. *J. Solid State Chem.* **1987**, *69*, 252.

(17) Pradel, A.; Pagnier, T.; Ribes, M. *Solid State Ionics* **1985**, *17*, 147.

(18) Mercier, R.; Malugani, J.-P.; Fahys, B.; Robert, G. *Solid State Ionics* **1981**, *5*, 663.

(19) Royle, M.; Cho, J.; Martin, S. W. *J. Non-Cryst. Solids* **2001**, *279*, 97.

(20) Wada, H.; Menetrier, M.; Levasseur, A.; Hagenmuller, P. *Mater. Res. Bull.* **1983**, *18*, 189.

(21) Creus, R.; Sarradin, J.; Astier, R.; Pradel, A.; Ribes, M. *Mater. Sci. Eng.: B* **1989**, *3*, 109.

(22) Yamashita, M.; Yamanaka, H.; Wakabayashi, H. *Solid State Ionics* **1996**, *89*, 299.

(23) Makimura, Y.; Rougier, A.; Tarascon, J.-M. *Appl. Surf. Sci.* **2006**, *252*, 4587.

(24) Bates, J. B.; Dudney, N. J.; Neudecker, B.; Ueda, A.; Evans, C. D. *Solid State Ionics* **2000**, *135*, 33.

(25) Kim, Y.-L.; Lee, H.-Y.; Jang, S.-W.; Lee, S.-J.; Baik, H.-K.; Yoon, Y.-S.; Park, Y.-S.; Lee, S.-M. *Solid State Ionics* **2003**, *160*, 235.

(26) Joo, K. H.; Vinatier, P.; Pecquenard, B.; Levasseur, A.; Sohn, H. J. *Solid State Ionics* **2003**, *160*, 51.

(27) Yamashita, H. Y. M.; Akai, T.; Wakabayashi, H. *Bull. Gov. Ind. Res. Inst. Osaka* **1991**, *42*, 208.

(28) Kim, Y.; Saienga, J.; Martin, S. W. *J. Non-Cryst. Solids* **2005**, *351*, 3716.

(29) Itoh, K.; Sonobe, M.; Mori, K.; Sugiyama, M.; Fukunaga, T. *Phys. B* **2006**, *385*−*386*, 520.

(30) Cunningham, P. T.; Johnson, S. A.; Cairns, E. J. *J. Electrochem. Soc.* **1972**, *119*, 1448.

(31) Komiya, R.; Hayashi, A.; Morimoto, H.; Tatsumisago, M.; Minami, T. *Solid State Ionics* **2001**, *140*, 83.

(32) Murayama, M.; Kanno, R.; Kawamoto, Y.; Kamiyama, T. *Solid State Ionics* **2002**, *154*−*155*, 789.

(33) Bourderau, S.; Brousse, T.; Schleich, D. M. *J. Power Sources* **1999**, *81*, 233.

(34) Cernosek, Z.; Cernosková, E.; Benes, L. *J. Mol. Struct.* **1997**, *435*, 193.

(35) Zhou, Z. H.; Kamiya, K.; Tsutsumi, K.; Hashimoto, T.; Nasu, H. *Phys. Chem. Glasses* **1999**, *40*, 146.

(36) Frumarova, B.; Oswald, J.; Krecmer, P.; Frumar, M.; Cerny, V.; Smrcka, V. *Opt. Mater.* **1996**, *6*, 217.

(37) Barrau, B.; Ribes, M.; Maurin, M.; Kone, A.; Souquet, J.-L. *J. Non-Cryst. Solids* **1980**, *37*, 1.